Two-Scale Model and Ocean Radar Doppler Spectra at Moderate- and Low-Grazing Angles

Valery U. Zavorotny and Alexander G. Voronovich

***Abstract*—Results of numerical calculations of polarized radar Doppler spectra from the ocean surface at low-grazing angles and at various wind speeds are presented. Calculations are based on the modified two-scale model, which includes Bragg scattering from both free and bound capillary waves. Here, we derive an analytical expression for the Doppler spectrum in the form of a two-dimensional (2-D) integral over large-scale slopes. For the surface description, the model of a directional wave spectrum is used, which takes into account the wave age (a limited fetch). A comparison of computed curves with experimentally measured Doppler spectra shows that the inclusion of "fast" bound capillary waves significantly improves results. Using the reasonable parameter values for the model of bound waves we obtained widths of Doppler spectra which are in good agreement with experiments for low-grazing angles $\theta_g = 10^\circ$ and for winds up to $U_{10} \sim 10$ m/s. However, remaining discrepancies show that using Bragg scattering from bound waves is not enough to close the problem. Despite of limitations the approach can be used for a more thorough analysis of measured Doppler spectra in order to determine the contributions of various scattering mechanisms.**

***Index Terms*—Sea surface electromagnetic scattering.**

I. Introduction

THE phenomenon of low-grazing scattering from a rough sea surface has attracted much attention, both experimentally and theoretically (see, e.g., [1]–[11]). This subject is of practical importance in areas of the low-altitude/long-range radar ocean remote sensing or target tracking, communication, and navigation systems operating at low-grazing conditions above the ocean surface. On the other hand, the observations at low-grazing angles (particularly, in the backscattering direction) differ from what the classical theoretical models (a small perturbation method, or a two-scale composite model) based on the Bragg-scattering mechanism predict for those angles. The key property of the low-grazing microwave backscattering is that for co-polarized emitted and received signals the radar cross section at horizontal polarization sometimes may attain or exceed the level of the vertically polarized signal. Another crucial difference lies in the shape of Doppler spectra (especially at horizontal polarization) for a low-grazing backscattering signal compared with those for a steep incidence.

Manuscript received April 15, 1997; revised August 19, 1997. This work was supported by the joint NOAA/DOD—Advanced Sensor Application Program.

The authors are with Cooperative Institute for Research in Environmental Sciences, University of Colorado/NOAA, Environmental Technology Laboratory, Boulder, CO 80303 USA.

Publisher Item Identifier S 0018-926X(98)01036-9.

The most practical tool for the theoretical description of rough surface scattering until now has been the two-scale (or composite) surface model [13]–[15]. As it was found by Trizna [12], although the two-scale model based on linear hydrodynamics appears to account for the peak Doppler shift of the spectrum for vertical polarization, it is insufficient to describe horizontally and cross-polarized data, which have larger Doppler shifts. For the case of moderate- and low-incidence angles Doppler spectra calculations based on the two-scale model and a comparison with experimental data were reported in papers [17]–[20]. Recently, Lee *et al.* [4], [5] explain their measured low-grazing angle Doppler spectra by coexistence of scatterers producing "slow signals" at frequencies close to the Bragg resonance with "fast scatterers" associated with breaking wave crests. Apparently, for some patches of an ocean surface the Bragg-scattering mechanism continues to work even at low-grazing angles contributing to the total backscattering signal. At the same time, close to unity polarization ratios of the "fast signals" suggest that some non-Bragg scatter from "fast scatterers" should be involved in the process.

While the theoretical description of non-Bragg scattering is still a subject for disputes, we intend to study the role of the Bragg component in Doppler spectra at low-grazing angles using our version of the two-scale model of the moving ocean surface. Here, we present a detailed derivation of an analytical expression for the polarized radar Doppler spectrum from an ocean surface, results of numerical computations based on it, and discuss their relevance to low-grazing-angle backscatter by a comparison with experimental data.

II. Two-Scale Model

We consider an electromagnetic (EM) wave incident on a dielectric moving rough surface, the mean position of which is at the $\vec{\rho} = (x, y)$ plane, the elevation of which above the plane is given by the equation $z = h(\vec{\rho}, t)$. Wave vectors of incident and scattered waves are in the (x, z) plane with the z axis directed upward (see Fig. 1). According to the basic concept of the composite model, the total rough-surface elevation is

$$h(\vec{\rho}, t) = h_1(\vec{\rho}, t) + h_2(\vec{\rho}, t) \tag{1}$$

where $h_1(\vec{\rho}, t)$ is a large-scale (in comparison to the EM wavelength λ) surface component which supposedly acts as a smooth facet within its characteristic scale. $h_2(\vec{\rho}, t)$ is a small-scale roughness superimposed on the large-scale one and statistically independent at different facets. The fact that facets

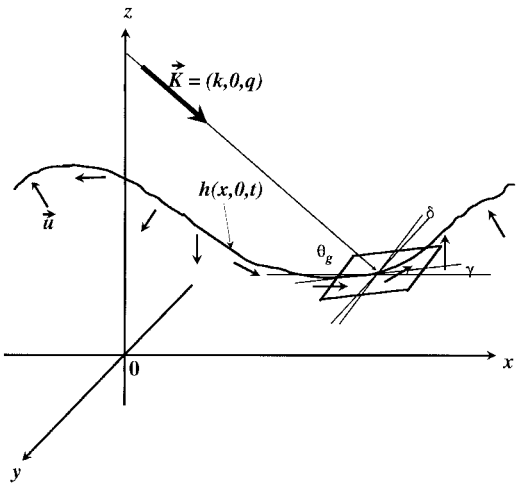

Fig. 1. Scattering geometry of a two-scale moving sea surface.

are curved rather than planar might be a significant matter in X-band backscattering for low-grazing angles. In [10], estimations and numerical calculations of curvature effects are made assuming that the modulation effect of facet tilts can be neglected. For this ideal case curvature effects begin to show up for grazing angles $\theta_g \lesssim 10°$–$20°$. However, when the effect of facet tilts is included assuming the realistic sea-roughness spectrum, the considerable curvature effects (about 5-dB increase) occur only for $\theta_g \lesssim 5°$ [11]. The calculations show that at the nominal grazing angle $\theta_g \sim 10°$ scattering from steep facets (with smaller curvature effects) dominates over that from sloping ones (with stronger curvature effects). Here, we shall consider $\theta_g \geq 10°$ and assume that the effect of facet curvatures can be excluded from discussion.

In terms of spatial spectra, the splitting presented by (1) can be reformulated as follows:

$$W(\vec{\kappa}) = W_1(\vec{\kappa}) + W_2(\vec{\kappa}) \tag{2}$$

where $W(\vec{\kappa})$ is the entire spatial spectrum of surface roughness, $W_1(\vec{\kappa}) = W(\vec{\kappa})\theta(\kappa_* - \kappa)$ is a low-frequency part that forms the large-scale undulating surface, $W_2(\vec{\kappa}) = W(\vec{\kappa})\theta(\kappa - \kappa_*)$ is a high-frequency part, and κ_* is a scale-dividing parameter (here, $\kappa = \left|\vec{\kappa}\right|$ and $\theta(\kappa)$ is a step-function). Tilts of the large-scale surface component can be characterized by the variance of related slopes s

$$\sigma^2_{s_{x,\,y}} = \left\langle s^2_{x,\,y} \right\rangle = \int\int \kappa^2_{x,\,y} W_1(\vec{\kappa}) d^2\kappa. \tag{3}$$

The high-frequency part $W_2(\vec{\kappa})$ should comply with two requirements. First, it should embrace the range of spatial frequencies satisfying the Bragg backscattering condition

$$\kappa = \kappa_B = 2K\,\cos\,\theta'_g \tag{4}$$

where θ'_g is the local grazing angle. Second, the Rayleigh criterion $K\sigma_{h_2}\,\sin\,\theta'_g \ll 1$ should be satisfied. Here $\sigma^2_{h_2} \equiv \int\int W_2(\vec{\kappa}) d^2\kappa$ is the height variance of the small-scale roughnesses. Within these limits, it is believed that the choice of κ_* is arbitrary.

III. Doppler Spectrum in a Two-Scale Surface Model

Now we turn to a consideration of an ocean-like moving surface. In this case, according to a chosen range of spatial scales, a small-scale roughness $h_2(\vec{\rho}, t)$ describes capillary (or gravity-capillary) surface waves propagating in all directions. Let the EM wave with wave vector $\vec{K} = (k, 0, q) = K(\cos\,\theta_g, 0, -\sin\,\theta_g)$ illuminate the tilted facet of a large-scale gravity wave where θ_g is the grazing angle for the incident EM wave with regard to the mean surface plane (see Fig. 1). Notice that $\tan\,\theta_g = q/k$. The tilts of facets can be described by the two-dimensional (2-D) slope vector $\vec{s} = (s_x, s_y) \approx \nabla h_1(\vec{\rho}, t)$ where $s_x = \tan\,\gamma$, $s_y = \tan\,\delta$, and γ is a facet-tilt angle in the plane of incidence x–z, and δ is a facet-tilt angle in the perpendicular plane. Also assume that the facet itself moves at a speed $\vec{u} = (u_x, u_y, u_z)$. For ocean-surface gravity waves this motion is associated with an orbital velocity of the surface water layer. In this case, the frequency of the EM wave scattered in the backward direction is

$$\omega = \omega_0 \pm \omega_B + 2\vec{K}\cdot\vec{u} \equiv \omega_0 + \omega_1^{\pm},\ \omega_B = c_B\kappa_B. \tag{5}$$

Here, ω_0 is a frequency of the incident EM wave and ω_B, κ_B, c_B are, respectively, the frequency, the wave number, and the phase speed of the Bragg resonant gravity-capillary wave. The sign $\pm$ accounts for approaching or receding waves. It is assumed in what follows that (5) is written for the case when the mean velocity of ocean water is equal to zero relative to the radar. In the presence of a steady drift (i.e., radar motion, currents or wind drift), one needs to introduce into (5) an additional Doppler shift. As a consequence of the two-scale model the total Doppler shift $\omega_1^{\pm} = \pm\omega_B + 2(ku_x + qu_z)$ consists of two terms. The first is caused by intrinsic velocities of small-scale Bragg-resonant waves and another one is produced by orbital motions associated with a large-scale component.

We now assume that Bragg-resonant waves can be of two types: "slow" and "fast." For a description of "slow" ones the following dispersion relation of linear (free) gravity-capillary waves is used here:

$$c_B = c_B^{sl}(\kappa_B) = \sqrt{g/\kappa_B + T\kappa_B/\varrho} \tag{6}$$

where g is gravitation acceleration, T is surface tension, and ϱ is the water density. We choose further for surface tension $T = 73$ dyne/cm, and for water density $\varrho = 1$ g/cm^3. For "fast" scatterers we assume that they are presumably associated with bound (parasitic) capillary waves generated at the front face of nonlinear gravity waves in the vicinity of their crests [2]. Thus, the velocity of the bound wave is assumed to be close to the phase velocity of the corresponding nonlinear gravity wave

$$c_B = c_B^f(\kappa_{nl}) \approx \sqrt{g/\kappa_{nl}}, \qquad \text{where} \quad \kappa_{nl} \ll \kappa_B. \tag{7}$$

For the purpose of our numerical simulations the wave number of the nonlinear gravity wave κ_{nl} was chosen by matching calculated curves with experimental radar data [5]. Clearly, the effect of orbital motions on "fast" scatterers should be determined by large-scale components with $\kappa < \kappa_{nl}$.

Hence, the scale-dividing parameter κ_* for this type of scatter has to be κ_{nl}.

As mentioned above, the two-scale scattering model postulates that the resultant cross section of the entire two-scale surface is a cross section of a single facet averaged over facet-tilt statistics. The same is true for the frequency spectrum of the backscattering signal. Averaging over the statistical ensemble of facets obviously results in the following equation for the frequency or Doppler spectrum of the backscattering signal:

$$F(\omega) = \int P\left(\vec{s}, \vec{u}\right)\left[\sigma^{+}(\vec{s})\delta\left(\omega - \omega_0 - \omega_1^{+}\right) + \sigma^{-}(\vec{s})\delta\left(\omega - \omega_0 - \omega_1^{-}\right)\right] d^2s d^3u. \tag{8}$$

Here, $\sigma^{\pm}(\vec{s})$ is the Bragg backscattering cross section that depends on the relative orientation of the incident wave and a facet and on the direction of resonant waves; $P\left(\vec{s}, \vec{u}\right)$ is an appropriate joint probability density function of the slope vector $\vec{s}$ and the vector of orbital velocity $\vec{u}$. One should remember that according to our concept the cross section $\sigma^{\pm}$ is a sum of two terms; σ^{sl} for "slow" (free) and σ^{f} for "fast" (bound) resonant waves. The cross section is also dependent on the polarization state of the transmitted and received EM wave. We shall introduce subscripts referring to a specific polarization later. The total backscattering cross section is

$$\sigma \equiv \int F(\omega)d\omega = \int P\left(\vec{s}\right)\left[\sigma^{+}(\vec{s}) + \sigma^{-}(\vec{s})\right] d^2s \tag{9}$$

where $P\left(\vec{s}\right) = \int P\left(\vec{s}, \vec{u}\right) d^3u$ is the probability density distribution of slopes only.

Technically, it is more convenient to have the probability density $P\left(\vec{s}, \vec{u}\right)$ in (8) represented in terms of corresponding characteristic function $\widetilde{P}$

$$P\left(\vec{s}, \vec{u}\right) = (2\pi)^{-5} \int d^2\zeta \int d^3\xi \widetilde{P}(\vec{\zeta}, \vec{\xi}) e^{i\left(\vec{\zeta}\cdot\vec{s} + \vec{\xi}\cdot\vec{u}\right)}. \tag{10}$$

Substituting (10) into (9) and performing obvious integrations as a result, one obtains

$$F = \int \left[\sigma^{+}(\vec{s})M^{+}\left(\vec{s}, \omega\right) + \sigma^{-}(\vec{s})M^{-}\left(\vec{s}, \omega\right)\right] d^2s \tag{11}$$

where

$$M^{\pm} = (2\pi)^{-5} \int d^2\zeta \int d^3\xi \int d^3u\delta\left(\omega - \omega_0 - \omega_1^{\pm}\right) \times \widetilde{P}(\vec{\zeta}, \vec{\xi}) \exp\left[i\left(\vec{\zeta}\cdot\vec{s} + \vec{\xi}\cdot\vec{u}\right)\right]. \tag{12}$$

Further, for a description of the long wave component, $h_1(\vec{\rho}, t)$, we limit our consideration by Gaussian statistics. In this case $\widetilde{P}$ is determined completely by correlation functions of slopes and orbital velocities. We also assume that the incidence plane of the EM wave lies in the wind direction. Then

$$\widetilde{P} = \exp\left[-\frac{1}{2}\left(\sigma_{s_x}^2\zeta_x^2 + \sigma_{s_y}^2\zeta_y^2 + \sigma_{u_x}^2\xi_x^2 + \sigma_{u_y}^2\xi_y^2 + \sigma_{u_z}^2\xi_z^2 + 2\langle s_x u_z\rangle\zeta_x\xi_z + 2\langle s_y u_z\rangle\zeta_y\xi_z\right)\right]. \tag{13}$$

Here, $\sigma_{s_i}^2$, and $\sigma_{u_i}^2$ are variances of i components of a slope vector s and of an orbital velocity u, respectively. Also here, we have correlations of some $\vec{s}$ and $\vec{u}$ components. For the Gaussian form of function $\widetilde{P}$ presented by (13) the integrals in (12) can be evaluated explicitly as

$$M^{\pm} = \frac{1}{2}\frac{1}{\sigma_{s_x}\sigma_{s_y}\sigma_{u_x}\sqrt{2\pi D}} \times \exp\left\{-\frac{1}{2D}\left[\left(1 + (\nu^2 - N_{yz}^2)\tan^2\theta_g\right)\tau_x^2 + \left(1 + (\nu^2 - N_{xz}^2)\tan^2\theta_g\right)\tau_y^2 + 2\nu^2\tan^2\theta_g N_{xz}N_{yz}\tau_x\tau + \left(1 + (\nu^2 - N_{xz}^2)\tan^2\theta_g\right)\tau_y^2 + \left(\frac{\Delta\omega^{\pm}}{2k\sigma_{u_x}}\right)^2 - \frac{\Delta\omega^{\pm}}{k\sigma_{u_x}}\nu\tan\theta_g(N_{xz}\tau_x + N_{yz}\tau_y)\right]\right\}. \tag{14}$$

Here

$$\nu = \sigma_{u_z}/\sigma_{u_x}, \quad N_{ij} = \langle s_i u_j\rangle/\sigma_{u_i}\sigma_{u_j} \cdot \tau_i = s_i/\sigma_{u_i}, \quad \Delta\omega^{\pm} = \omega - \omega_0 \mp \omega_B \tag{15}$$

and

$$D = 1 + \nu^2(1 - N_{xz}^2 - N_{yz}^2)\tan^2\theta_g. \tag{16}$$

IV. A Model of the Surface Large-Scale Component

To continue the analysis let us derive variances and correlators of slopes and velocities obtained in the above equations. Here we shall assume first that the large-scale surface $h_1(\vec{\rho}, t)$ can be described by a statistically homogeneous, stationary ensemble of linear propagating waves with sufficiently small slopes

$$h_1(\vec{\rho}, t) = \frac{1}{\sqrt{2}}\int \left(a_\kappa e^{i\vec{\kappa}\cdot\vec{\rho} - i\omega_\kappa t} + a_\kappa^* e^{-i\vec{\kappa}\cdot\vec{\rho} + i\omega_\kappa t}\right) d^2\kappa \tag{17}$$

where a_κ is a complex Fourier amplitude with the wave vector $\vec{\kappa}$, ω_κ as its frequency, and the asterisk indicates a complex conjugation. For gravity waves $\omega_\kappa^2 = g\kappa$, where $\kappa = \left|\vec{\kappa}\right|$. We also assume that nonlinear effects resulting in the appearance of bound waves are small enough to be neglected below in the calculations of correlators associated with large-scale waves. Spatial homogeneity of the statistical ensemble yields

$$\langle a_\kappa a_{\kappa'}\rangle = \langle a_\kappa^* a_{\kappa'}^*\rangle = 0 \tag{18}$$

and

$$\langle a_\kappa a_{\kappa'}^*\rangle = \Psi_1(\vec{\kappa})\delta(\vec{\kappa} - \vec{\kappa}\,') \tag{19}$$

where angle brackets stands for statistical ensemble averaging and $\Psi_1(\vec{\kappa})$ is the directional wavenumber spectrum of $h_1(\vec{\rho}, t)$ [21]. Indeed, the spectrum Ψ (or $\Psi_{1,2}$) satisfies to the relationship

$$\Psi(\vec{\kappa}) = 2\int_0^\infty X(\vec{\kappa}, \omega)d\omega \tag{20}$$

where

$$X(\vec{\kappa}, \omega) = \frac{1}{(2\pi)^3}\int_{-\infty}^{\infty} d^2\rho \int_{-\infty}^{\infty} dt e^{-i\left(\vec{\kappa}\cdot\vec{\rho}-\omega t\right)} \times \left\langle h(\vec{r}, t_0)h(\vec{r}+\vec{\rho}, t_0+t)\right\rangle \tag{21}$$

is the wave spectrum for a statistically homogeneous, stationary wave field $h(\vec{\rho}, t)$ [21]. The directional spectrum $\Psi(\vec{\kappa})$ is connected to the spectrum $W(\vec{\kappa})$ introduced in (2) by the relation

$$W(\vec{\kappa}) = \tfrac{1}{2}[\Psi(\vec{\kappa}) + \Psi(-\vec{\kappa})]. \tag{22}$$

Note that the power spectrum $W(\vec{\kappa})$ arises from the time-independent spatial analysis, which does not contain actual wave-propagation information, whereas the spectrum $\Psi(\vec{\kappa})$ represents the wavenumber directional (here, in $\pm$ directions) distribution of wave-energy propagation. From the above equations it follows that the spectrum $\Psi(\vec{\kappa})$ is normalized according to the relation $\sigma_h^2 \equiv \langle h^2\rangle = \int \Psi(\vec{\kappa})d^2\kappa$. Using well-known relations for linear surface waves, one easily obtains from (17)

$$\vec{s} = \frac{i}{\sqrt{2}}\int \vec{\kappa}\left(a_\kappa e^{i\vec{\kappa}\cdot\vec{\rho}-i\omega_\kappa t} - a_\kappa^* e^{-i\vec{\kappa}\cdot\vec{\rho}+i\omega_\kappa t}\right) d^2\kappa \tag{23}$$

$$\vec{u}_\perp = \frac{1}{\sqrt{2}}\int \frac{\omega_\kappa \vec{\kappa}}{|\kappa|}\left(a_\kappa e^{i\vec{\kappa}\cdot\vec{\rho}-i\omega_\kappa t} + a_\kappa^* e^{-i\vec{\kappa}\cdot\vec{\rho}+i\omega_\kappa t}\right) d^2\kappa \tag{24}$$

$$u_z = -\frac{i}{\sqrt{2}}\int \omega_\kappa\left(a_\kappa e^{i\vec{\kappa}\cdot\vec{\rho}-i\omega_\kappa t} - a_\kappa^* e^{-i\vec{\kappa}\cdot\vec{\rho}+i\omega_\kappa t}\right) d^2\kappa. \tag{25}$$

Upon squaring and averaging we obtain the parameters needed for the function P

$$\sigma^2_{s_{x,y}} = \left\langle s^2_{x,y}\right\rangle = \int\int \kappa^2_{x,y}\Psi_1(\vec{\kappa})d^2\kappa \tag{26}$$

$$\sigma^2_{u_{x,y}} = \left\langle u^2_{x,y}\right\rangle = \int \frac{\kappa^2_{x,y}}{|\kappa|^2}\omega_\kappa^2\Psi_1(\vec{\kappa})\, d^2\kappa \tag{27}$$

$$\sigma^2_{u_z} = \left\langle u_z^2\right\rangle = \int \omega_\kappa^2\Psi_1(\kappa)\, d\kappa \;\equiv\; \sigma^2_{u_x} + \sigma^2_{u_y} \tag{28}$$

and

$$\left\langle \vec{s}\, u_z\right\rangle = -\int \vec{\kappa}\omega_\kappa \Psi_1(\vec{\kappa})\, d^2\kappa. \tag{29}$$

For a statistically homogeneous surface, $\left\langle \vec{s}\cdot\vec{u}_\perp\right\rangle = \langle u_x u_z\rangle = \langle u_y u_z\rangle = 0$.

V. Backscattering Cross Section from Tilted Facet

The function needed for calculations of the integral in (11) is $\sigma^{\pm}(\vec{s})$, a backscattering cross section of a tilted facet. The expression for this value is well-known (see e.g., [16]):

$$\sigma^{\pm}_{HH}(\vec{s}) = 4\pi K^4 \sin^4\theta'_g \left|\left(\frac{a\cos\delta}{b}\right)^2 g_\perp(\theta'_g) + \left(\frac{\sin\delta}{b}\right)^2 g_\parallel(\theta'_g)\right|^2 \Psi_2(\mp 2Ka,\, \mp 2Kd\sin\delta) \tag{30}$$

$$\sigma^{\pm}_{VV}(\vec{s}) = 4\pi K^4 \sin^4\theta'_g \left|\left(\frac{a\cos\delta}{b}\right) g_\parallel(\theta'_g) + \left(\frac{\sin\delta}{b}\right)^2 g_\perp(\theta'_g)\right|^2 \Psi_2(\mp 2Ka,\, \mp 2K\, d\sin\delta) \tag{31}$$

where

$$a = \cos(\theta_g+\gamma), \quad b = \cos\theta'_g$$
$$d = \sin(\theta_g+\gamma), \quad \theta'_g = \arcsin(d\cos\delta). \tag{32}$$

Here, the sign $\pm$ indicates the direction of the approaching and receding Bragg-resonant waves. Subscripts HH and VV stand for horizontal- and vertical-polarization cases, respectively. Remember that the angle θ_g is a grazing angle for the incident EM wave with regard to the mean-surface plane, whereas the angle θ'_g is a local grazing angle between wave vector $\vec{K}$ and the plane of a facet. The angle γ is a facet-tilt angle in the plane of incidence, x–z, and δ is a facet-tilt angle in the perpendicular plane. Coefficients $g_\perp$ and $g_\parallel$ in (30) and (31) are defined as follows:

$$g_\perp(\theta'_g) = \frac{\varepsilon-1}{\left[\sin\theta'_g + \sqrt{\varepsilon-\cos^2\theta'_g}\right]^2} \tag{33}$$

$$g_\parallel(\theta'_g) = \frac{(\varepsilon-1)\left[\varepsilon(1+\cos^2\theta'_g) - \cos^2\theta'_g\right]}{\left[\varepsilon\sin\theta'_g + \sqrt{\varepsilon-\cos^2\theta'_g}\right]^2} \tag{34}$$

where ε is the complex dielectric constant of a sea water.

Equations (30) and (31) for an elementary cross section at two polarizations include the directional spectrum $\Psi_2(\kappa_x, \kappa_y)$ of the Bragg-resonant component $h_2(\vec{\rho}, t)$. A dependence on κ_y appears here due to a facet tilting out of the plane of incidence.

VI. Model for the Surface Spectrum

In the calculations to be presented below, we have assumed an improved model for the surface spectrum, which accounts for recently discovered features as the high-frequency spectral bump [22] and the wave-age dependence typical for developing or young seas, which takes place under limited fetch conditions (see, e.g., [23]). This model contains one important parameter—the inverse wave age

$$\Omega = U_{10}/c_p \equiv U_{10}\sqrt{\kappa_d/g} \tag{35}$$

where U_{10} is the wind velocity at a height of 10 m, c_p is the phase speed of the dominant wave, which corresponds to the spectral peak, κ_d is the wavenumber of the dominant wave. For example, for a well-developed sea, $\Omega = 0.83$, and for young seas, $\Omega \sim$ 2–3. There is strong experimental

support that for $0.83 < \Omega < 5$, the energy-containing part of the spectrum depends on the wave age [23]. At the same time, the wave-age dependence of the high wave-number spectrum is a controversial issue [24]. Taking into account these circumstances, we adopt what we call here the modified Donelan–Banner–Jähne spectrum, which is based on models discussed in [22]–[24]

$$\Psi(\kappa, \phi) = A L_0(\kappa)\Gamma^{\gamma(\kappa)}\kappa^{-4} H_i(\kappa) D(\kappa, \phi) \tag{36}$$

where

$$A = 0.002\,16\,\Omega^{0.55} \tag{37}$$

$$L_0(\kappa) = \exp\left[-(\kappa_d/\kappa)^2\right] \tag{38}$$

$$\Gamma = 1.7 + 6\log\Omega \tag{39}$$

$$\gamma(\kappa) = \exp\left[-(\kappa^{1/2} - \kappa_d^{1/2})^2/2\delta^2\kappa_d\right] \tag{40}$$

$$\delta = 0.08(1 + 4\,\Omega^{-3}) \tag{41}$$

$$H_i(\kappa) = [R_{ro} + SR_{\rm res}]V_{\rm dis} \tag{42}$$

$$R_{ro} = [1 + (\kappa/\kappa_{ro})^2]^{-1} \tag{43}$$

$$S = \exp\left\{[3.45(1 - \exp(-U_{10}/U_\eta) - 4.95]\ln 10\right\} \tag{44}$$

$$R_{\rm res} = 0.8\,\kappa\,\mathrm{sech}[(\kappa - \kappa_{\rm res})/\kappa_w] \tag{45}$$

$$V_{\rm dis} = \exp\left[-(\kappa/\kappa_{\rm dis})^2\right] \tag{46}$$

$$D = \mathrm{sech}^2\{[(0.4 + 2.28(\kappa/\kappa_p)^{-0.65}](\phi - \phi_U)\} \tag{47}$$

$$\kappa_d = g(\Omega/U_{10})^2. \tag{48}$$

Dimensional numerical constants in (43)–(45) and (46) are $\kappa_{ro} = 100$ rad/m, $\kappa_{\rm res} = 400$ rad/m, $\kappa_w = 450$ rad/m, $\kappa_{\rm dis} = 6283$, $U_\eta = 4.7$ m/s, and ϕ_U in (47) is the angle of wind direction in radians. Upon substitution of $\Omega = 0.83$ into (37), (39), and (41) we obtain expressions for a case of the well developed spectrum considered by Apel [22].

To account for the presumed presence of bound waves we set

$$H_i(\kappa) = H_i^{sl}(\kappa) + H_i^f(\kappa) \tag{49}$$

$$H_i^{sl}(\kappa) = (1 - \mu)H_i(\kappa); \quad H_i^f(\kappa) = \mu H_i(\kappa) \tag{50}$$

where μ is a share of "fast" (bound) waves in the total elevation spectrum. As it was mentioned above the phase speed of bound waves coincides with the phase speed of the primary gravity wave which depends on κ_{nl} [see (7)]. To account for a possible spread of the κ_{nl} value the following model for the distribution function is adopted:

$$P(\kappa_{nl}) = \begin{cases} 0, & \text{if } \kappa_{nl} < \kappa_d \text{ and } \kappa_{nl} > \kappa_1 \\ (\kappa_{nl} - \kappa_d)(\kappa_0 - \kappa_d), & \text{if } \kappa_d \le \kappa_{nl} \le \kappa_0 \\ (\kappa_1 - \kappa_{nl})/(\kappa_1 - \kappa_d), & \text{if } \kappa_0 < \kappa_{nl} \le \kappa_0 \end{cases} \tag{51}$$

where κ_0 denotes a position of the distribution maximum. The distribution is confined between κ_d, the elevation spectrum peak position, and the high-frequency cutoff κ_1. Therefore, in our model for bound waves exist three free parameters μ, κ_0, and κ_1. Because they are not available from measurements reported in [4] and [5], their rough estimates were obtained by fitting calculated Doppler spectra with measured ones. Of course, the spectral model of bound waves presented above by (42)–(51) is introduced here in a pure phenomenological *ad hoc* manner and further, more rigorous approaches would be welcomed.

TABLE I
ENVIRONMENTAL DATA

θ_g, deg	10	10	10	35	35
ϕ_U, deg	180	180	180	180	0
U_{10}, m/s	3.8	6.0	10.3	9.5	10.5
$f_{\rm dom}$, Hz	0.70	0.65	0.43	0.55	0.48
Ω	1.70	2.50	2.84	3.35	3.23
v_b, m/s	1.30	1.20	1.05	0.80	1.15
v_w, m/s	0.11	0.18	0.31	0.59	-0.10
κ_d, rad/m	1.97	1.70	0.74	-	-
μ	0.1	0.1	0.5	0	0
κ_0, rad/m	65.1	7.5	1.9	-	-
κ_1, rad/m	65.8	48.4	12.2	-	-

VII. NUMERICAL RESULTS AND COMPARISON WITH EXPERIMENT

Because our intention was to compare calculations with experimental data from [4] and [5], we must briefly describe the condition and geometry of the experiment. The data were obtained from a CW dual-polarized X-band (9.02–9.47 GHz) coherent scatterometer, which was mounted on an extended platform on the bow of a boat. Backscattering experiments were conducted off the west coast of Scotland in the summer of 1991. Time-resolved backscattered signals and their Doppler spectra were obtained from the ocean surface at a range of grazing angles from 10° to 70° and for a range of wind speeds. The contributions from both the boat speed and the wind drift were taken into account. Corresponding values can be found in our Table I. Series of Doppler spectra obtained at different wind directions and wind velocities show a transition from the conventional Bragg scattering to the less-studied scattering regimes. We chose to compare our numerical upwind/downwind calculations with data [4, Fig. 20], which depict Doppler spectra as a function of wind direction obtained at a fixed grazing angle of $\theta_g = 35°$. Another case for comparison is taken from [5, Fig. 3], which represents wind-speed dependence of upwind-looking Doppler spectra for a grazing angle of 10°.

We present here environmental data for both cases in our Table I. In this table θ_g is a grazing angle, ϕ_U is an angle between the positive x direction and wind direction shown in (36), U_{10} is the wind speed at 10 m above water level, f_d is the dominant wave frequency of the ocean wave-amplitude spectrum, related to κ_d from (35), v_b is the boat speed, and v_w is the wind drift. The inverse wave age Ω is calculated using (35) with U_{10} and f_d from Table I. Note that for our scattering geometry $\phi_U = 0°$ refers to the downwind direction and $\phi_U = 180°$ refers to the upwind direction. We should mention also that the scattering experiment cited appeared to be conducted at young seas rather than at well-developed ones. Data for the wind drift, v_w were available from [5] only for measurements at $\theta_g = 10°$. Values for v_w for $\theta_g = 35°$ were obtained here indirectly as a result of matching the peak positions taken from computations and from experimental Doppler spectra. Mention also that the wave-elevation spectrum presented in [5, Fig. 10] was obviously underestimated by the constant close to 19 dB, probably due to a normalization error.

Results presented below were obtained by numerical integration in (11) with use of (14), (30), and (31). For our

computations we used a radar wavelength $\lambda = 3.22$ cm (X-band) and a dielectric constant for sea water $\varepsilon = 51.4 + i39.1$, values reported in [4]. Also, we took into account that what was mentioned as grazing-angle direction is actually a bore-sight direction or direction of the maximum in the antenna pattern.

For calculating the "slow" component of Doppler spectra the scale-dividing parameter κ_* was chosen equal to $3k_B$, while for the case of "fast" component (as it was explained above), κ_* was chosen equal to κ_{nl}. An additional averaging over κ_{nl} was performed using the modeled distribution presented by (51). Numerical parameters of this distribution and the values of the bound wave share μ can be found in Table I. The numerical integration over tilts s in (11) was performed within ranges limited by $\pm 3\sigma_s$. To account for the near-crest position of bound waves at the front face of the gravity wave-carrier, these limits were shifted by $-30°$ when calculating "fast" component. At low-grazing angles, a shadowing of the surface by its large-scale excursions takes place. For simplicity, we treat this shadowing as a geometrical self-shadowing, which can be simulated in (11) by integration only over positive local slopes only, i.e., when $\tan\theta_g + s > 0$. Thus, backscattering from self-shadowed facets is completely excluded. However, shadowing due to neighboring surface excursions cannot be accounted for within a standard two-scale approach.

Curves presented on Fig. 2(a) and (b) shows Doppler spectra for the case of a moderate grazing angle $\theta_g = 35°$ in the upwind and in the downwind directions, respectively. Solid curves are experimental data from [4], dashed curves represent two-scale model calculations for the "slow" component . A contribution from bound waves was neglected in this case: $\mu = 0$. Thick and thin lines correspond to the VV and HH polarizations, respectively. The theoretical curves were calculated assuming the modified Donelan–Banner–Jähne spectrum from (36) and environmental data from Table I. Note that Doppler measurements and two-scale model calculations of ("slow" according to our terminology) Doppler spectra for the steep incidence ($\theta_g \sim 70°$) presented in previous studies [17], [18] demonstrate a quite good agreement. However, at $\theta_g = 35°$ our calculations based only on a "slow component" begin to show some departures from measured curves. The comparison of numerical curves and experimental ones in Fig. 2(a) and (b) shows that only for a downwind direction do we have a fair correspondence between the experiment and calculations for both polarizations in terms of peak values and spectral widths. The more pronounced departure between calculated and measured Doppler spectra appears at upwind direction [see Fig. 2(b)]. The peak value at the VV polarization is higher by about 10 dB than the computations give us. The width of the experimental spectrum is visually larger and the spectrum itself extends more toward higher frequencies than the calculated one. This makes it similar to what the Doppler spectra look like at smaller grazing angles.

Now we turn to the case of low-grazing angles $\theta_g = 10°$. This case is presented in a series of plots in Fig. 3(a)–(c), which were calculated for conditions presented in Table I. Here, we have upwind direction and U_{10} ranging from 3.8 to 10.3 m/s. Thick solid curves represent measured Doppler

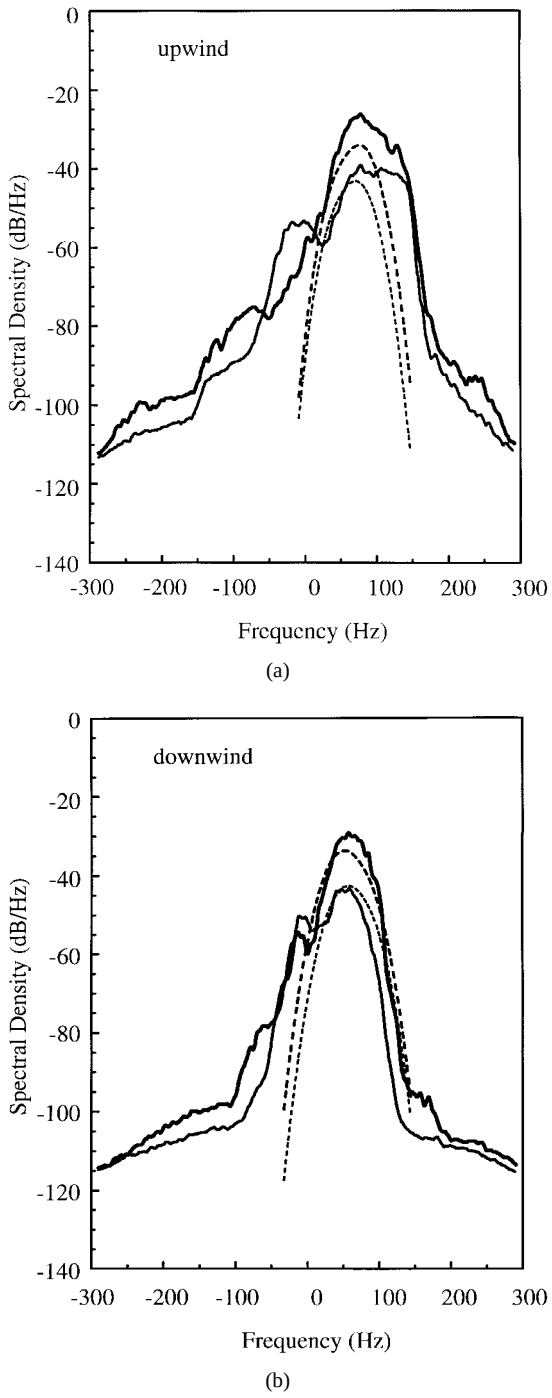

Fig. 2. Doppler spectra at (a) upwind and (b) downwind directions and at grazing angle $\theta_g = 35°$. Solid curves are experimental data from [4], dashed curves represent two-scale model calculations for the "slow" component $\mu = 0$. Thick and thin lines correspond to the VV- and HH-polarizations, respectively.

spectra. Dashed curves represent two-scale model calculations for the "slow" component of Doppler spectra (without bound waves $\mu = 0$), while thin solid curves correspond to "slow + fast" spectra (with bound waves $\mu \neq 0$). Upper three curves correspond to the VV polarization and lower three curves correspond to the HH polarization.

A better fit (for both $\mu = 0$ and $\mu \neq 0$ cases) is observed at weaker winds, which is reasonable. Also, for weak winds

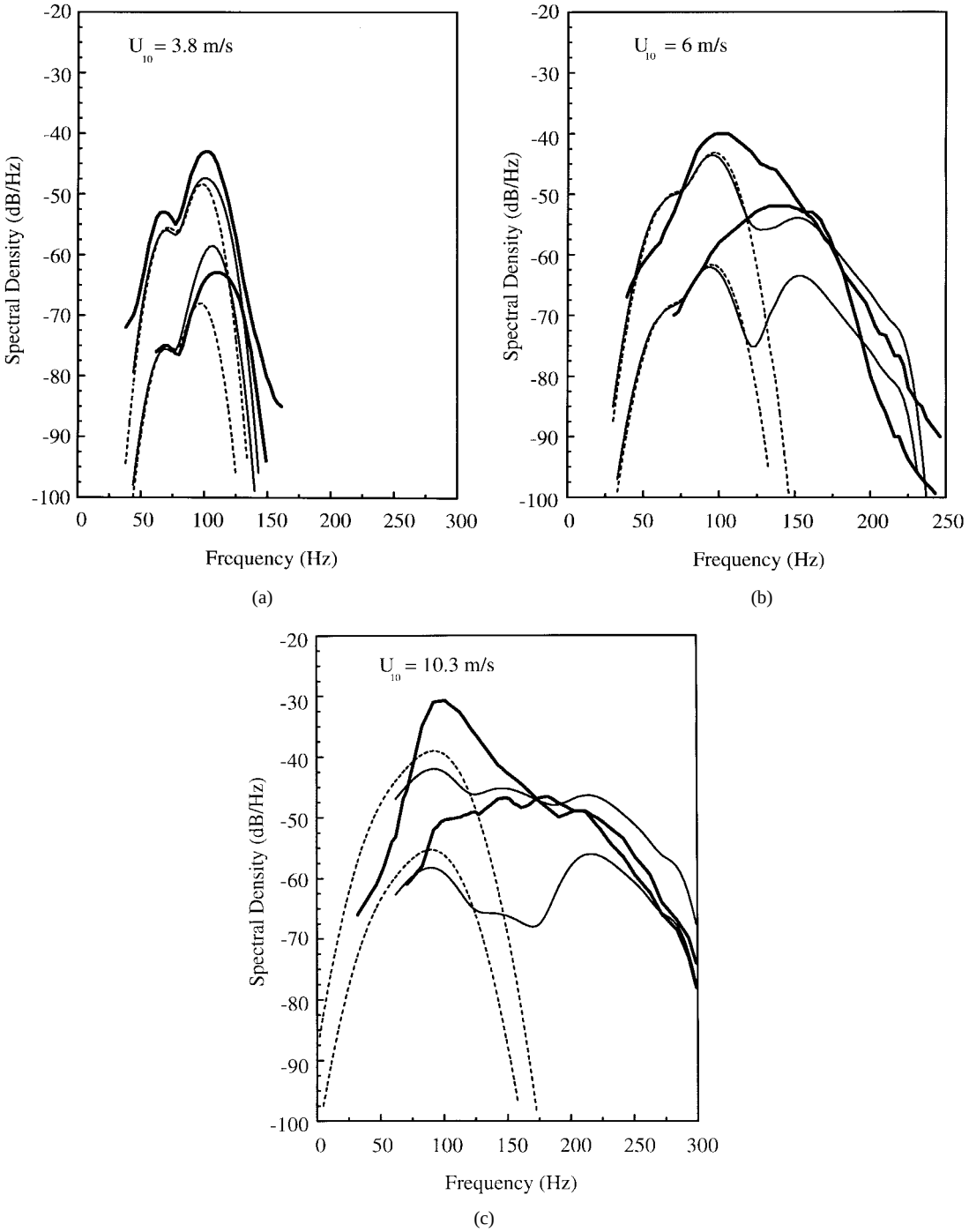

Fig. 3. Doppler spectra as a function of wind velocity [from panels (a)–(c)] at the upwind direction and at grazing angle $\theta_g = 10°$. Thick solid curves represent experimental data from [5], dashed curves represent two-scale model calculations for the "slow" component $\mu = 0$ thin solid curves represent two-scale model calculations for the "slow + fast" spectrum $\mu \neq 0$. Upper three curves correspond to the VV polarization and lower three curves correspond to the HH polarization.

one can see a bimodal shape both for calculated and measured spectra. For the surface with free capillary waves only and without large-scale components, the Doppler spectrum of the backscattered signal would have consisted of two narrow separate peaks: one at Bragg resonant frequency f_B^+ for approaching capillary waves and another at Bragg resonant frequency f_B^- for receding capillary waves. The difference between amplitudes for these two peaks is determined by the angular dependence $D(\kappa, \phi)$ in (47). For the case presented in Fig. 3(a) this difference is about 7.4 dB. Inclusion of large-scale components immediately leads to an appearance of orbital motions associated with these components. For strong enough winds and developed seas these motions generate much larger values of the orbital velocity compared to the phase velocity c_p. As a result, orbital velocities should spread out those Bragg peaks, and the width of the Doppler spectrum would be determined by the variance of the corresponding component of orbital velocity. For higher winds this variance

exceeds the difference $f_B^+ - f_B^-$ and the Doppler spectra become unimodal.

For $U_{10} = 3.8$ m/s [Fig. 3(a)] lower frequency parts of calculated spectra have a good match at the HH polarization with a somewhat lower position for the calculated VV-polarization curve. Peak positions match for the VV polarization at expected Bragg resonant frequencies f_B^+ and f_B^-. One can see that an inclusion of the "fast" component can improve results especially for the HH polarization. On Fig. 3(b) and (c) the positions of the single peak near f_B^+ for VV spectra, measured and calculated (even for the case of the "slow" component only), are in a good agreement, and for HH spectra they are not, which coincides with the conclusion made by Trizna [12]. A significant widening and buildup of measured Doppler spectra is seen at frequencies $f \gtrsim f_B^+$ on Fig. 3(b) and (c). The widening can be explained by scattering by "fast" bound waves. A rather good agreement with experimental data in this regard was achieved for reasonable values of parameters μ, κ_0, and κ_1 (see Table I). The buildup, however, cannot be explained by this mechanism only and it can be partially attributed to the growing contribution from the non-Bragg scattering from steep and curved roughnesses. Of course, this mechanism is out of the scope of the two-scale model presented here. However, it is instructive to see what part of measured spectrum still can be assigned to chosen here mechanisms and models and what part needs more advanced theory.

VIII. Conclusions

We have presented the results of numerical calculations of polarized radar Doppler spectra from the ocean surface in upwind and downwind directions at $\theta_g = 35°$ and for various wind speeds in an upwind direction and at $\theta_g = 10°$. These calculations are based on the modified two-scale model, which includes Bragg scattering from both free and bound capillary waves and their random modulation by tilts and orbital motions produced by large-scale components of gravity waves. The latter process is described by making use of linear wave theory and Gaussian statistics for those large-scale waves. The final expression for the Doppler spectrum is obtained in the form of a 2-D integral over large-scale slopes. This expression includes such second-order statistical parameters as variances of slope components, variances of orbital velocity components, their correlations, and power spectra of surface elevations at Bragg-resonant frequencies. For the surface statistical description we invoke models of directional wave spectra, which take into account the effect of wave age.

In experiments [4], [5] it was found that at low-grazing angles (and sometimes even at moderate-grazing angles) two different mechanisms are responsible for the formation of the Doppler spectrum. One relates to the low-frequency part of the spectrum ("slow signal") presumably caused by the Bragg scattering from free capillary waves; another relates to the high-frequency part of the spectrum ("fast signal") due to the some other mechanisms. The two-scale model used here is assigned to describe effects related to the Bragg scattering from both free and bound resonant waves. Therefore, our intention was to check which spectral features may and which may not be explained by the theory developed here. Using the reasonable parameter values for the model of bound waves we obtained widths of Doppler spectra, which are in good agreement with experiments for low grazing angles $\theta_g = 10°$ and for winds up to $U_{10} \sim 10$ m/s. However, this model cannot account for the entire buildup of the Doppler spectra at frequencies $f \gtrsim f_B^+$ for higher winds $U_{10} \gtrsim 6$ m/s. A more elaborate and self-consistent hydrodynamic model together with more advanced theory for non-Bragg scattering from steep roughnesses is obviously desirable. Despite of evident limitations the presented here approach can be used for a more thorough analysis of measured Doppler spectra in order to determine the contributions of various scattering mechanisms.

Acknowledgment

The authors would like to thank P. H. Y. Lee of TRW Space & Electronics, Redondo Beach, CA, for useful discussions, A. V. Smirnov of CIRES/NOAA/ETL, Boulder, CO, for valuable assistance, and two anonymous referees for helpful comments.

References

[1] R. A. Kropfli and S. F. Clifford, "The San Clemente ocean probing experiment: A study of air-sea interactions with remote and *in situ* sensors," in *Int. Geosci. Remote Sensing Symp. Conf. Proc.*, Pasadena, CA, Aug. 1994, vol. IV, pp. 2407–2409.

[2] A. D. Rozenberg, D. C. Quigley, and W. K. Melville, "Laboratory study of polarized scattering by surface waves at grazing incidence: Part I–Wind waves," *IEEE Trans. Geosci. Remote Sensing* vol. 33, pp. 1037–1046, July 1995.

[3] A. V. Smirnov and V. U. Zavorotny, "Study of polarization differences in K_u-band ocean radar imagery," *J. Phys. Oceanography*, vol. 25, pp. 2215–2228, 1995.

[4] P. H. Y. Lee, J. D. Barter, K. L. Beach, C. L. Hindman, B. M. Lake, H. Rungaldier, J. C. Shelton, A. B. Williams, R. Yee, and H. C. Yuen, "X-band microwave backscattering from ocean waves," *J. Geophys. Res.*, vol. 100, pp. 2591–2611, 1995.

[5] P. H. Y. Lee, J. D. Barter, E. Caponi, M. Caponi, C. L. Hindman, B. M. Lake, and H. Rungaldier, "Wind-speed dependence of small-grazing-angle microwave backscattering from sea surfaces," *IEEE Trans. Antennas Propagat.*, vol. 44, pp. 333–340, Mar. 1996.

[6] J. D. Barter and P. H. Y. Lee, "Polarimetric optical imaging of scattering surfaces," *Appl. Opt.*, vol. 35, pp. 6015–6027, 1996.

[7] D. B. Trizna and D. J. Carlson, "Studies of dual polarized low grazing angle radar sea scatter in nearshore regions," *IEEE Trans. Geosci. Remote Sensing*, vol. 34, pp. 747–757, May 1996.

[8] C. L. Rino, E. Eckert, A. Siegel, T. Webster, A. Ochadlick, M. Rankin, and J. Davis, "X-band low-grazing-angle ocean backscatter obtained during LOGAN 1993," *IEEE J. Oceanic Eng.*, vol. 22, pp. 18–26, Jan. 1997.

[9] D. E. Barrick, "Near-grazing illumination and shadowing of rough surfaces," *Radio Sci.*, vol. 30, pp. 563–580, 1995.

[10] A. G. Voronovich, "On the theory of electromagnetic waves scattering from the sea surface at low grazing angles," *Radio Sci.*, vol. 31, pp. 1519–1530, 1996.

[11] A. G. Voronovich and V. U. Zavorotny, "Curvature effects in the composite model for low grazing angle rough-surface scatter," *Waves Random Media*, to be published.

[12] D. B. Trizna, "A model for Doppler peak spectral shift for low grazing angle sea scatter," *IEEE J. Oceanic Eng.*, vol. OE-10, pp. 368–375, Oct. 1985.

[13] B. F. Kur'yanov, "The scattering of sound at a rough surface with two types of irregularity," *Sov. Phys. Acoust.*, vol. 8, pp. 252–257, 1963.

[14] J. W. Wright, "A new model for sea clutter," *IEEE Trans. Antennas Propagat.*, vol. AP-16, pp. 217–223, Feb. 1968.

[15] F. G. Bass, I. M. Fuks, A. I. Kalmykov, I. E. Ostrovsky, and A. D. Rozenberg, "Very high frequency radiowave scattering by a disturbed sea surface 2: Scattering from an actual sea surface," *IEEE Trans. Antennas Propagat.*, vol. AP-16, pp. 560–568, May 1968.

[16] G. R. Valenzuela, "Theories for the interaction of electromagnetic and oceanic waves—A review," *Boundary Layer Meteorol.*, vol. 31, pp. 61–85, 1978.
[17] D. R. Thompson, "Doppler spectra from the ocean surface with a time-dependent composite model," in *Radar Scattering From Modulated Wind Waves*, G. J. Komen and W. A. Oost, Eds. Norwell, MA: Kluwer, 1989, pp. 27–40.
[18] D. R. Thompson, B. L. Gotwols, and W. C. Keller, "A comparison of K_u-band Doppler measurements at 20° incidence with predictions from a wave-current interaction model," *J. Geophys. Res.*, vol. 96, pp. 4947–4955, 1991.
[19] M. B. Kanevskii and V. Ya. Karaev, "Spectrum of radar signal reflected from sea surface," *Radiophys. Quantum Electron.*, vol. 36, pp. 1–9, 1993.
[20] Y. V. Grebenyuk, M. B. Kanevskii, and V. Yu. Karaev, "Doppler spectrum width of microwave radar signals reflected from sea surface at moderate and large incidence angles," *Izvestiga Russian Academy Sci. Atmospheric Oceanic Phys.*, vol. 30, pp. 57–60, 1994.
[21] M. L. Banner, "Equilibrium spectra of wind waves," *J. Phys. Oceanography*, vol. 20, pp. 966–984, 1990.
[22] J. P. Apel, "An improved model of the ocean surface wave vector spectrum and its effects on radar backscatter," *J. Geophys. Res.*, vol. 99, pp. 16269–16291, 1994.
[23] M. A. Donelan, J. Hamilton, and W. H. Hui, "Directional spectra of wind generated waves," *Philosophical Trans. Royal Soc. London*, vol. 315, pt. A, pp. 509–562, 1985.
[24] V. K. Makin, V. N. Kudryavtsev, and C. Mastenbroek, "Drag of the sea surface," *Boundary Layer Meteorol.*, vol. 73, pp. 159–182, 1995.

Valery U. Zavorotny was born in Chernovtsy, Ukraine. He received the M.S. degree in radio physics from Gorky State University, Gorky, Russia, in 1971, and the Ph.D. degree in geophysics from the Institute of Atmospheric Physics of USSR Academy of Sciences, Moscow, in 1979.

From 1971 to 1990, he was a Research Scientist with the Institute of Atmospheric Physics of USSR Academy of Sciences, Moscow. In 1990 he joined Lebedev Physical Institute, Moscow, Russia. Since 1991, he has been a Research Scientist with University of Colorado's Cooperative Institute for Research in Environmental Sciences and the Environmental Technology Laboratory of the National Oceanic and Atmospheric Administration (NOAA), Boulder, CO. His research interests include wave scattering from rough surfaces, optical and radio wave propagation through random media, ocean and atmospheric remote sensing techniques.

Dr. Zavorotny is a member of the Optical Society of America.

Alexander G. Voronovich was born in Moscow, Russia. He received the M.S. degree in physics and the Ph.D. degree in theoretical and mathematical physics, both from Moscow Institute of Physics and Technology, Moscow, USSR, in 1972 and 1975, respectively, and the Doctor of Science degree in theoretical and mathematical physics from the Acoustical Institute, Moscow, in 1988.

From 1975 to 1979, he was a Junior Research Scientist in the Acoustical Institute, Moscow. In 1980, he joined P. P. Shirshov Institute of Oceanology, Moscow, Russia, as a Senior Research Scientist, and became a full Professor of physics at Moscow Institute of Physics and Technology in 1991. From 1989 to 1993 he was a Head of the Laboratory of Acoustical Waves Propagation in the Ocean of the P. P. Shirshov Institute of Oceanology. He is currently a Research Scientist with University of Colorado's Cooperative Institute for Research in Environmental Sciences and the Environmental Technology Laboratory of the National Oceanic and Atmospheric Administration (NOAA), Boulder, CO. His research interests include wave scattering from rough surfaces, ocean acoustics, geophysical hydrodynamics, internal waves, and linear and nonlinear theory of wave propagation.

Dr. Voronovich is a Fellow of the Acoustical Society of America.